Seismic attenuation imaging of Campi Flegrei: Evidence of gas reservoirs, hydrothermal basins, and feeding systems

L. De Siena,[1,2] E. Del Pezzo,[1] and F. Bianco[1]

[1]   Passive high-resolution attenuation tomography is used here to image the geological structure in the first upper 4 km of the shallow crust beneath the Campi Flegrei caldera, southern Italy. The inverse Q was estimated for each source-receiver path using the coda-normalization method (S-waves) and the slope decay method (P-waves and S-waves). Inversion was performed using a multi-resolution method, which ensures a minimum cell-size resolution of 500 m. The study of the resolution matrix as well as the synthetic tests guarantee an optimal reproduction of the input anomalies in the center of the caldera, between 0 and 3.5 km in depth. High attenuation vertical structures are connected at the surface with the main volcanological features (e.g., the Solfatara and Mofete fumarole fields), and depict vertical Q contrast imaging important geological structures, such as the La Starza fault. These high attenuation volumes extend between the surface and a depth of about 3 km, where a hard rock layer is imaged by the sharp contrast of the quality factors. The retrieved image of the Campi Flegrei has been jointly interpreted taking into account evidence from seismological, geological, volcanological and geochemical investigations. This analysis has allowed an unprecedented view of the feeding systems in this area, and in particular it recognizes the vertically extending, high attenuation structures that correspond to gas or fluid reservoirs beneath Pozzuoli-Solfatara, Solfatara, Mofete-Mt. Nuovo and Agnano. This high-attenuation system is possibly connected with the magma sill revealed at about 7 km in depth by passive travel-time tomography.

1.   Introduction

[2]   From a seismological point of view, volcanic areas are complex structures that are characterized by solidified intrusions, partially molten regions, geothermally altered rocks, and intricate deposits of different shapes, thicknesses and compositions. Passive high resolution tomography is a widely used method for the important task of imaging the internal structures of volcanoes; this in turn represents a crucial step towards the correct constraints for the eruption models [*Chouet*, 1996]. Travel-time tomography is the most commonly used approach to obtain detailed images [*Chouet*, 2003]. Attenuation imaging has been used less, despite an increasing number of studies on this subject [*Schurr et al.*, 2003; *Hansen et al.*, 2004; *Eberhart-Phillips et al.*, 2005; *De Gori et al.*, 2005]. Recently, multiscale algorithms have been introduced to obtain the best resolution according to the optimal robustness and stability of the procedures

[*Bai and Greenhalgh*, 2005; *De Siena et al.*, 2009]. Auxiliary Material.[1]

[3]   The attenuation of elastic waves depends on a number of factors, the most important of which are the temperature and the presence of fractures that are generally permeated by fluids [*Eberhart-Phillips et al.*, 2005]. Attenuation is quantified by the quality factor, Q, which is defined as the ratio between the energy lost by a wave cycle and the energy of the cycle itself. Similarly, attenuation can be defined through the attenuation coefficient, $\alpha = \pi fr/vQ$, which accounts for the damping of the wave amplitude, A, as a function of distance, r, and frequency, f. The α coefficient can vary by a significant amount for rocks sharing the same chemical composition and different temperatures and/or degrees of fracturing. In addition, the response of the rocks to the propagation of longitudinal waves is different to that for shear waves; consequently, knowledge of Q_P and Q_S, the P-wave and S-wave quality factors, respectively, is crucial for the characterization of the physical state of the rocks inside a volcano.

[4]   Scattering is a physical process that intensely affects the wave propagation in volcanic areas and tends to transfer the high-frequency energy of direct P-waves and S-waves

---

[1]Istituto Nazionale di Geofisica e Vulcanologia, Naples, Italy.
[2]Also at Institute for Geophysics, University of Münster, Münster, Germany.

[1]Auxiliary materials are available in the HTML. doi:10.1029/2009JB006938.

into the coda of the seismograms [*Sato and Fehler*, 1998]. Scattering effects are produced by the interactions of the wavefield with the small scale heterogeneities in the elastic parameters, such as, for example, those associated with intense rock fracturing. The attenuation caused by scattering can be estimated independently of the intrinsic dissipation [*Del Pezzo et al.*, 2006b]. Unfortunately, in single-path estimates of the attenuation coefficient (necessary for tomography), separation between the scattering and intrinsic contributions is practically impossible; in attenuation tomography, the seismic attribute is the total $Q(Q_T)$, or the corresponding attenuation coefficient. This is a limit for unequivocal interpretations of the attenuation imaging; as an example, focusing-defocusing effects [*Nolet*, 2008] are not distinguishable from the scattering attenuation effects at the spatial scale of our inversion, and are included in Q_T. A wide range of physical properties must be considered in discussing the results of velocity and/or attenuation tomography, and their combined interpretation is a decisive tool in discriminating volumes permeated by fluids and/or by structural discontinuities [*Nakajima and Hasegawa*, 2003]. The spatial variation of V_P mirrors the distribution of lithologies and rock properties, while the V_P/V_S ratio maps rock defects, pores and cracks, and their fluid contents. Fluid-filled pores in matrix rocks result in a decrease in both V_P and V_S while variations in V_P/V_S of a matrix rock including fluids depends not only on the kind of fluids, but also on the shape of the pores [*Nakajima and Hasegawa*, 2003; *Schmeling*, 1985; *Takei*, 2002]. Ambiguous interpretations of the causes of seismic velocity anomalies can be removed by a joint interpretation with Q_P^{-1} and Q_S^{-1} measures: as an example, Q_P^{-1} can be used to discriminate between water-filled media and gas reservoirs [*Hansen et al.*, 2004], while high attenuation anomalies are a strong clue for the presence of melt-filled inclusions, which are always characterized by high *Vp/Vs* [*Takei*, 2002].

[5] In the present study, we have obtained a three-dimensional (3-D) compressional- and shear-wave attenuation structure of the Campi Flegrei volcano near Naples, southern Italy, using a multi-scale approach associated with site independent estimate of the seismic attributes (coda-normalization method). This approach allows the retrieval of images with unprecedented high resolution (500 meters cell size) in the areas of maximum volcanological interest. Previous attempts in the same area [*De Lorenzo et al.*, 2001] obtained P-wave images in a smaller investigation volume at a resolution of 1000 meters cell size.
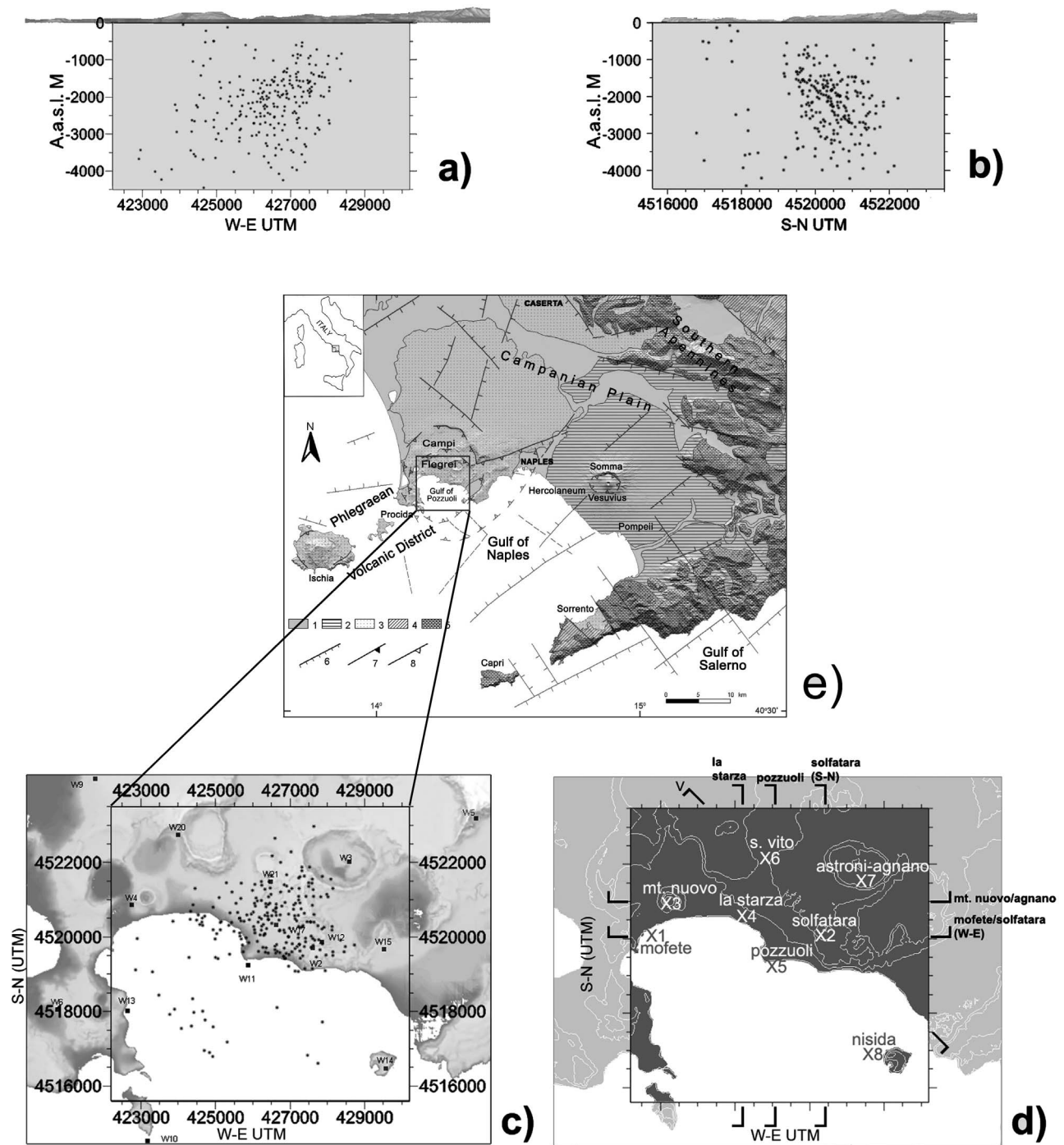
2. Data, Velocity Model, and Ray Tracing

[6] The Campi Flegrei volcanic area is located inside the Campanian Plain, west of the city of Naples, where a marked lithospheric thinning has been observed [*Di Renzo et al.*, 2007] (Figure 1e). The graben-like structure of the caldera is assumed to be mostly due to the collapse following the Campanian Ignimbritic eruption (about 35000 years ago) and its second period of activity (14,000–10,500 years ago), when Neapolitan yellow tuff covered a large part of the area [*Scandone et al.*, 1991; *Orsi et al.*, 1996]. A third period of strong activity produced an uplift of the northern sector of the Gulf of Pozzuoli, which was probably due to shallow magma injection. There were successive eruptions until the one that

resulted in the formation of Mt. Nuovo [*Di Vito et al.*, 1987], which occurred near the local geomorphological discontinuity that is commonly known as "La Starza" [*Di Vito et al.*, 1999], as shown in Figure 1d. Three main episodes of slow vertical ground uplift (bradyseism) have been recognized over the last 40 years [see, e.g., *Saccorotti et al.*, 2007, and references therein]. The first two of these were between 1950 and the early 1970 s, while the third one occurred in 1982–1984. The second and the third episodes produced a maximum vertical displacement of 1.7 and 1.6 meters, respectively, and were associated with strong seismic activity [*Corrado et al.*, 1976; *Berrino et al.*, 1984].

[7] The present database is composed of 246 earthquakes that occurred during the seismic crisis at Campi Flegrei from January to June 1984 and were recorded at 15 three-component seismic stations (Table 1), deployed by the University of Wisconsin and equipped with three-component, short-period sensors, sampled at 100 or 200 s.p.s. The data set used in the present study has been used in the past in many studies on several aspects of Campi Flegrei seismicity, and has been widely described together with their quality [see, e.g., *Pujol and Aster*, 1990, and references therein]. The vertical and horizontal registrations of three events of our data set with similar source-station distance are reported in Figure 2, as well as P-, S- and coda-spectra and the corresponding single path Q_P and Q_S estimates. Herein, we represent these data (e.g., source location), the velocity and attenuation images in a WE and SN reference system, with the origin at the sea level and the z axis positive upward. As an example, in this system, −1000 means a depth of 1000 m. In total, 853 waveforms were selected (for each component), considering the best signal-to-noise ratios, the absence of spikes and other disturbances, a minimum coda duration (from origin time) of 15 s, and the absence of secondary events in the early coda. In making this selection, we have implicitly restricted the magnitude in the range from 1.8 to 3.0. We measured the corner frequency, calculating the intersection between the straight lines fitting the logarithmic low-frequency and high-frequency spectrum, respectively. We have also tested whether the retrieved corner frequencies coincide with those obtained by fitting the observed spectra with the theoretical spectral shape function in the uncertainty interval.

[8] The first velocity models of Campi Flegrei were obtained using the data recorded in 1982–1984 [*Aster and Meyer*, 1988, 1989; *Pujol and Aster*, 1990]. Recently, these data were combined with data obtained by a high resolution offshore reflection survey (the SERAPIS Project) that took place in 2001 into the Gulf of Pozzuoli [*Zollo et al.*, 2006], which greatly improved the quality of the images and their interpretation. *Battaglia et al.* [2008] obtained a velocity model of Campi Flegrei for P-waves and S-waves by merging passive and active data sets of travel-times that were obtained during the 1984 seismic crisis and the 2001 SERAPIS experiment, respectively. Their methods used an improved finite difference travel-time computation, jointly inverting the velocity model and the event locations by means of a weighted damped least squares approach. Their minimum cell size was 250 m, well inside the minimum cell size used in the present study. Due to this difference in the spatial resolution, the smearing effects possibly affecting the

Figure 1. (a and b) W-E and S-N vertical sections of the seismicity pattern at Campi Flegrei. (c) Map of Campi Flegrei with the station positions (black squares) and hypocenter locations (stras) for the seismic events indicated. (d) Map of Campi Flegrei with the area investigated in the present study highlighted. The names and the capital letter (V) at the upper and eastern sides of the area define the spatial locations of the vertical sections for which the tomographic images in Figures 7 are shown. (e) Geological and structural sketch map of the Southern Campanian Plain (modified after *Di Renzo et al.* [2007]). 1, Quaternary and active terrigenous sediments; 2, Somma-Vesuvius volcanic deposits; 3, Phlegraean, Procida and Ischia volcanic deposits; 4, Pliocene and Miocene terrigenous sediments; 5, Mesozoic carbonate units; 6, fault; 7, overthrust; 8, caldera rim. The gray square borders the area under investigation.

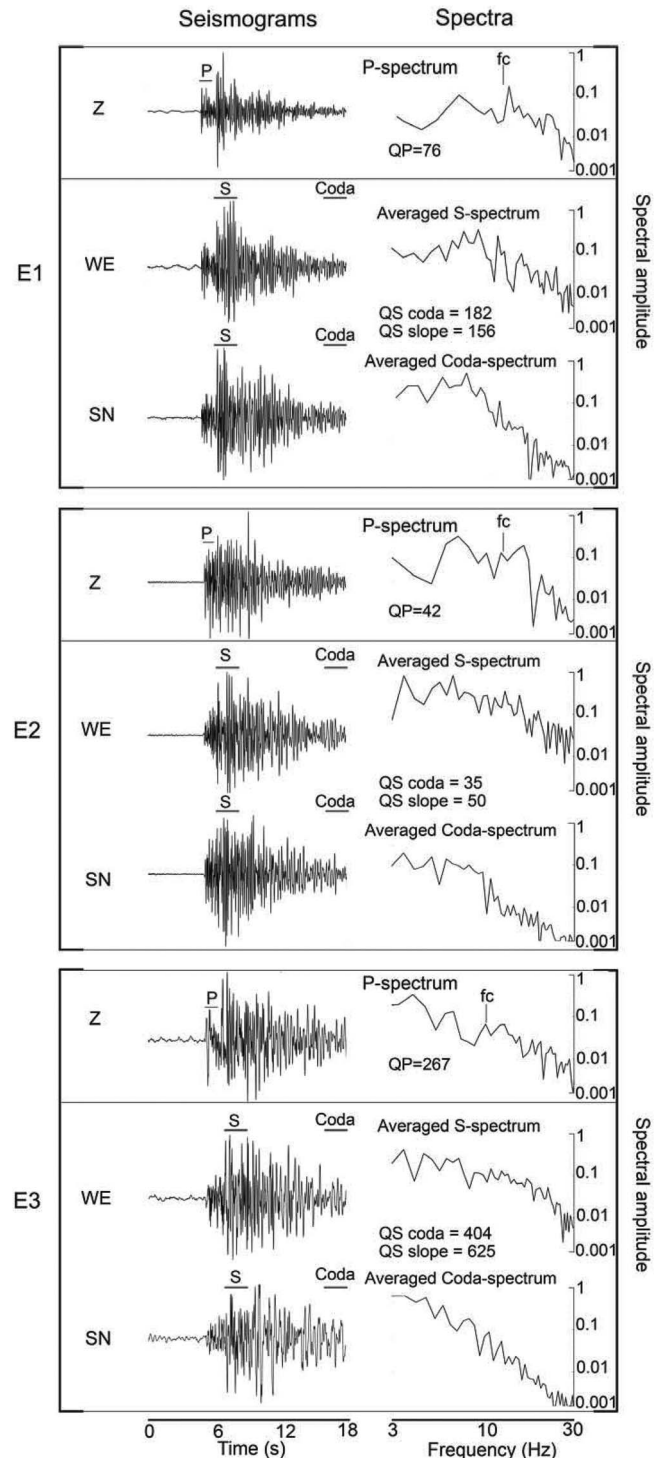**Table 1.** The 15 Three-Component Seismic Stations for Data Collection in the Present Study

Station	E-W (UTM)	N-S (UTM)
W02	427566	4519739
W03	428526	4522058
W04	422726	4520835
W05	431901	4523261
W06	420763	4518016
W09	421708	4524328
W10	423200	4514502
W11	425836	4519261
W12	427812	4519891
W13	422626	4518002
W14	429552	4516520
W15	429466	4519724
W17	426579	4520335
W20	423932	4522742
W21	426425	4521502

velocity images might not strongly contaminate our interpretation based on the joint comparison of attenuation and velocity tomography. The velocity tomography results have depicted an annular high P-wave velocity anomaly, which is possibly the signature of the buried rim of the caldera. The V_P/V_S model revealed a high V_P/V_S anomaly under the city of Pozzuoli, around 1000 m in depth, and of a low V_P/V_S body laterally extending at about −4000 m, below a large part of the caldera. In the present study, we have used this model as the basis for ray tracing and for localization, as well as for comparing velocity and attenuation images.

[9] We have relocated the selected data set using a nonlinear localization algorithm [*Lomax et al.*, 2001], re-picking the P- and S-wave arrivals on all the available waveforms. The data confirm that most of the seismicity is located inland, while a small number of the events are under the sea in the bay (Figure 1c). The maximum accepted uncertainty associated with source coordinates is of the order of 300 meters. We have used a Thurber-modified bending approach to trace the path of each ray in the 3D velocity structure. This method is an extension of the approximate ray-bending method that has worked well in velocity structures characterized by relatively sharp velocity variations, like that of Campi Flegrei [*Block*, 1991]. After dividing the whole structure to be investigated into two different grids (of 1000 *m* and 500 *m* cell sizes), we calculated the lengths of each ray, connecting each source to each receiver, and the lengths of the ray segments crossing each cell. These data are needed for application of the multi-resolution inversion, previously applied and tested with a much larger data set recorded at Mt. Vesuvius [*De Siena et al.*, 2009]. The distribution of seismic sources at Campi Flegrei allows the retrieval of the attenuation images at a similar resolution (500 *m* versus 300 *m*) with one third of the waveforms number used at Mt. Vesuvius.

3. Single-Path S-Wave Attenuation: The Coda-Normalization Method

[10] The coda-normalization (CN) method is widely used to retrieve attenuation parameters independently of the site and instrumental transfer functions [*Aki*, 1980; *Sato and Fehler*, 1998]. *Del Pezzo et al.* [2006a] and *De Siena et al.* [2009] provided an extensive treatment of this approach and its application to attenuation tomography, and thus we

Figure 2. (left) The horizontal and vertical registrations of three events having similar source station distances, starting at the origin time of each event. The P-, S- and coda-windows used to measure spectra are indicated on each trace. (right) P- and averaged (on the two horizontal component) S- and coda-spectra. The corner frequency (fc) as well as the P- (*QP*) and S- wave (*QS CN*, *QS SD*) single path quality factors obtained with different methods are also indicated.

Table 2. Frequency Bands in Which the Results Have Been Obtained

$-\Delta f$	$f_c(Hz)$	$+\Delta f$
4	6	8
10	15	20

refer to their studies for a wider description of the method. The method is based on the equation that correlates the ratio between the S-wave direct energy ($E_{ij}(f, r)$) and the coda-wave energy ($E^C(f, t)$) to the spatial distribution of the total quality factors (Q_T^{ij}) calculated along the source (i)-station (j) ray-path. Using this procedure we obtain the following equation:

$$d_k^C = \frac{1}{2\pi f}\ln\left(\frac{\theta_{ij}(\vartheta, \phi)}{P(f, t_c)}\right) - \sum_{b=1}^{N\_cells} l_{kb} s_b Q_b^{-1} \quad (1)$$

where $d_k^C = \frac{1}{2\pi f}\ln(r^2 \frac{E_{ij}(f,r)}{E^C(f,t)})$, N_cells is the total number of blocks crossed by the ray, l_{kb} is the length of the k-th ray segment intersecting the b-th block, characterized by the slowness s_b and an inverse quality factor Q_b^{-1}. We use the suffix k to indicate the k-th ray belonging to the suite of rays connecting stations to sources. $\theta_{ij}(\vartheta, \phi)$ is the radiation pattern function, which depends on the source azimuth ϕ and incidence angle ϑ. $P(f, t_c)$ represents the coda envelope shape, calculated at the lapse time t_c. We set the coda signal time window starting with a 16 s lapse time and ending at 18 s, since most of our data show a favorable signal-to-noise ratio (>3) for lapse times smaller than 20 s. A discrete Fourier transform is applied to the signals after windowing (we used a cosine taper window with tapering at 10% for both S and the coda), for both the horizontal components of the ground motion. Then we smooth the spectra, averaging for the frequency bands centered at the values of frequency f_c, with bandwidths ($\pm\Delta f$) reported in Table 2. Finally, we log-average the horizontal component spectra, and calculate the ratio between the S-wave-averaged spectrum and the averaged coda spectrum. The natural logarithm of this ratio estimates the quantity d_k^C of equation (1). Our aim is to solve equation (1) for Q_b^{-1}. We smooth the radiation pattern effects by estimating $E_{ij}(f, r)$ in a time window containing the direct S-wave pulse plus the first 2 s of the early S-coda, which is formed by forward scattered S-wave radiation. It can be theoretically demonstrated that the effects of the radiation pattern decrease in the early coda with increasing lapse time [*Gusev and Abubakirov*, 1999]. We have checked experimentally that the radiation pattern effects are strongly reduced in the present data for a time window of 2 s, using a statistical change point test [*Mulargia and Tinti*, 1985]. A detailed description of this given by *De Siena et al.* [2009, Appendix 2]. Consequently, we can assume $\theta_{ij}(\vartheta, \phi) = 1$, and equation (1) becomes:

$$d_k^C = \frac{1}{2\pi f}\ln\left(\frac{1}{P(f, t_c)}\right) - \sum_{b=1}^{N\_cells} l_{kb} s_b Q_b^{-1} \quad (2)$$

[11] Equation (2) represents a linear system of N_k (the number of rays) equations in $N\_cells + 1$ unknowns. In this formulation we solve for the average scattering properties of

the medium (the constant $\frac{1}{2\pi f}\ln(\frac{1}{P(f, t_c)})$) and for the total inverse quality factor in each block.

4. Single-Path P-Wave Attenuation: The Ordinary Slope-Decay Method

[12] As is well known, the amplitude spectral densities for P-waves and S-waves can be expressed as the products of the source, path and site effects, as:

$$A_{ij}^{HF}(f, r) = S_i^A(f)I_j(f)T_j(f)G_{ij}(r)\exp\left(-\pi f \int_{rij} \frac{s(l)dl}{Q_T(l)}\right) \quad (3)$$

where $A^{HF}(f, r)$ is the high-frequency spectral amplitude of the P-wave or S-wave radiation emitted by the source i at a total distance r measured along the source(i)-station (j) ray-path; f is the frequency; $S_i^A(f)$ is the amplitude spectrum at source; I_j is the instrument transfer function; T_j is the site transfer function; G is the geometrical spreading term; and Q_T^{ij} is the total quality factor measured along the ray-path. In the present study, we use the formulation of *Abercrombie* [1995], assuming that the high-frequency amplitude spectrum at the source can be described by a function $S_i^A = \frac{\Omega_0}{[1+(f/f_{Corn})^{\gamma n}]^{1/\gamma}}$, where Ω_0 is the long-period amplitude, f_{Corn} the measured corner frequency, n the frequency (log-log) fall-off rate, and γ is a constant for the whole data set used. We have observed that the modified version of the spectral shape proposed by *Boatwright* [1980] ($n = 2$ and $\gamma = 2$) better fits the displacement spectra obtained from our data set. Following the formulation of *Anderson and Hough* [1984] and *Margaris and Boore* [1998] we factor the quantity $T(f)$ into equation (3) in the product of $T'(f)$, a path-independent site-transfer function, and a path-dependent term, $\exp(-k_0 f)$, where k_0 is a coefficient characteristic of the site. Taking the natural logarithm, making the derivative of the equation (3) with respect to frequency, and transforming the pairs of indices ij into a single integer k that is associated with the single ray, we can write:

$$D_f\left(\ln A_k^{HF}\right) = -2\frac{f^3}{f_{Corn}^4 + f^4} - \pi k_0 + D_f(\ln(T'(f)))$$
$$- \pi \sum_{b=1}^{N\_cells} l_{kb} s_b Q_b^{-1}, \quad (4)$$

where D_f is the symbol of the derivative. In obtaining equation (4), we have assumed independence of the frequency for the instrument transfer function, which is flat in the whole frequency range investigated, and we have approximated the integral with a sum, as in equation (1); indicating all the measured quantities with:

$$d_k^S = \frac{1}{\pi}\left[-D_f\left(\ln A_k^{HF}\right) - 2\frac{f^3}{f_{Corn}^4 + f^4} - \pi k_0 + D_f(\ln(T'(f)))\right], \quad (5)$$

we can write:

$$d_k^S = \sum_{b=1}^{N\_cells} l_{kb} s_b Q_b^{-1}. \quad (6)$$

Direct P spectral amplitudes were calculated in the frequency bands centered at $f_c = 6$ Hz and $f_c = 15$ Hz, with bandwidths ($\pm\Delta f$) (Table 2). A discrete Fourier transform is applied to a time window starting from the P-wave onset, and ending at 0.1 s before the S-wave picking, tapering each spectrum with a 10% cosine taper function. We log-average the spectra over the components, and use the results obtained in the same area by *De Natale et al.* [1987] and *Del Pezzo et al.* [1993], who measured path-independent and path-dependent site-effects in equation (5) to correct for these quantities. The derivatives of equation (5) are computed using the MATLAB "diffnew" routine. The inversion schemes (2) and (6) are formally identical, apart from the constant value.

5.   Multi-resolution Inversion

[13]   It is well known that the resolution of seismic imaging depends both on the wavelength (which should be smaller than the cell size) and the number of rays sampling the single cell [*Bai and Greenhalgh*, 2005]. In the present data set, a frequency of 6 Hz corresponds to a wavelength of about 250 m for S-waves and of about 500 m for P-waves. For the same data, the average Fresnel radius, which is calculated for the average ray length of 3.2 km, is less than 400 m for S-waves and less than 500 m for P-waves. Consequently, we assume a minimum cell size of 500 m, to obtain reliable results in the sub-volume with maximum number of hypocenters and ray coverage, and where the finite frequency effects are reasonably reduced. Outside this sub-volume, we assume a cell size of 1000 m. We use an iterative inversion scheme similar to the one used by *De Siena et al.* [2009], using the results obtained at a lower resolution as constraints for the problem at higher resolution. The seismic attributes are calculated both for the CN method and the slope-decay (SD) method. The procedure is described in the online materials. The solutions for the inverse problems described by equations (2) and (6) are obtained using the zero-th order Tikhonov regularization method [*Aster et al.*, 2005]. We selected a damping factor of 0.65 for the S and P low-resolution images (cell size of 1000 m) and of 0.09 for the high-resolution images (cell size of 500 m), considering the trade-off between model complexity and residuals variance from several one-step inversions. Formal errors in the final parameters calculated with the covariance matrices are less than 15 percent of the observed Q_S variations and 25 percent of the observed Q_P variations. The empirical equation used to evaluate the blocks effectively solved in the final inversion is:

$$n_R \geq \frac{4 Block\_side}{\lambda}. \tag{7}$$

where n_R is the number of ray-segments crossing the block, and λ is the wavelength at which we obtained the data.

n_R changes as a function of resolution, wave-type and frequency, as detailed in the online materials.

6.   Resolution Matrix Analysis, Checkerboard, and Synthetic Anomaly Tests

[14]   An appraisal of the resolution is essential for a meaningful interpretation of seismic tomography images. First, we exclude that the uncertainty associated with the source coordinates significantly affects the estimate of Q along the ray path. We tested this randomly perturbing the source coordinates inside their uncertainties and inverting the perturbed data set. Results were indistinguishable from unperturbed solutions. The diagonal terms of the resolution matrix (RDE) for both the Q_S^{-1} and Q_P^{-1} inversions at lower resolution (1000 m) were always greater than 0.5; less than 2% of the absolute values of the off-diagonal terms were larger than 0.1. So, the resolution of 1000 m is assumed as good everywhere, particularly in the central part of the model (RDE > 0.8), where the crossing rate is higher. For the maximum resolution (500 m), in the first rows of both Figure 3 and Figure 4, we show the output of the inversion procedures that represent the attenuation structure at different depths (columns, as indicated). The resolution matrix has been used to calculate the spreading function (SF), as defined by *Michelini and McEvilly* [1991]; the SF is shown in the second row of Figure 3 (S-waves) and of Figure 4 (P-waves), indicating where the well resolved-zones are located. In Figure 5 the two plots of the RDE versus the corresponding SF values are shown for each wave type. Following the procedure of *Dias et al.* [2007], the joint analysis of Figure 3 and Figure 5a reveals that for S-waves and a resolution of 500 m, an SF > 1.5 implies a very low resolution, while well-resolved nodes will have an SF < 1; the SF cut-off value will be located somewhere in between. The joint analysis of Figure 4 and Figure 5b shows that an adequate threshold value for P-waves will be located between 1 and 1.6. The P-wave inversion results are less resolved then the ones for S-waves, especially under the sea (e.g., the southern part of the caldera). To be anyway conservative, we do not consider as resolved the zones with SF > 1.1 for S-waves and SF > 1.4 for P-waves, corresponding to the white color in the corresponding figures. The presence of poorly solved cells is evident in the areas contouring the center of the caldera (second rows of Figure 3 and Figure 4). The S-wave and P-wave attenuation images under Solfatara, Mt. Nuovo, La Starza and Pozzuoli (Figure 3 and Figure 4, markers X2, X3, X4 and X5, respectively) are well resolved until −3200 m. The best resolution for S-waves is obtained under the La Starza fault and Pozzuoli (Figure 3 and Figure 4, markers X4 and X5). The S-wave attenuation image is best resolved in the central part of the caldera, at all depths: the best resolved zones for the P-waves are the

Figure 3.   Four horizontal sets of panels for S-waves intersecting the volume under study at different depths: (a) −200 m, (b) −1200 m, (c) −2200 m, and (d) −3200 m. The tomography results (first row), the spread function values at maximum resolution (second row), and the input and output of the checkerboard test (third and fourth rows) and the synthetic anomaly test (fifth and sixth rows) are shown in the same horizontal panels. The colored and gray scales (represented on the right of each row) show the variation from the average S-wave inverse quality factor. The sea coast is plotted as a white contour on each horizontal colored tomogram, with the locations of the area of great volcanological indicated as the following legend: X1, Mofete; X2, Solfatara; X3, Mt. Nuovo; X4, La Starza; X5, Pozzuoli; X6, San Vito; X7, Agnano; X8, Nisida. The bold black dashed lines roughly contour the maximum resolution areas (500 m).
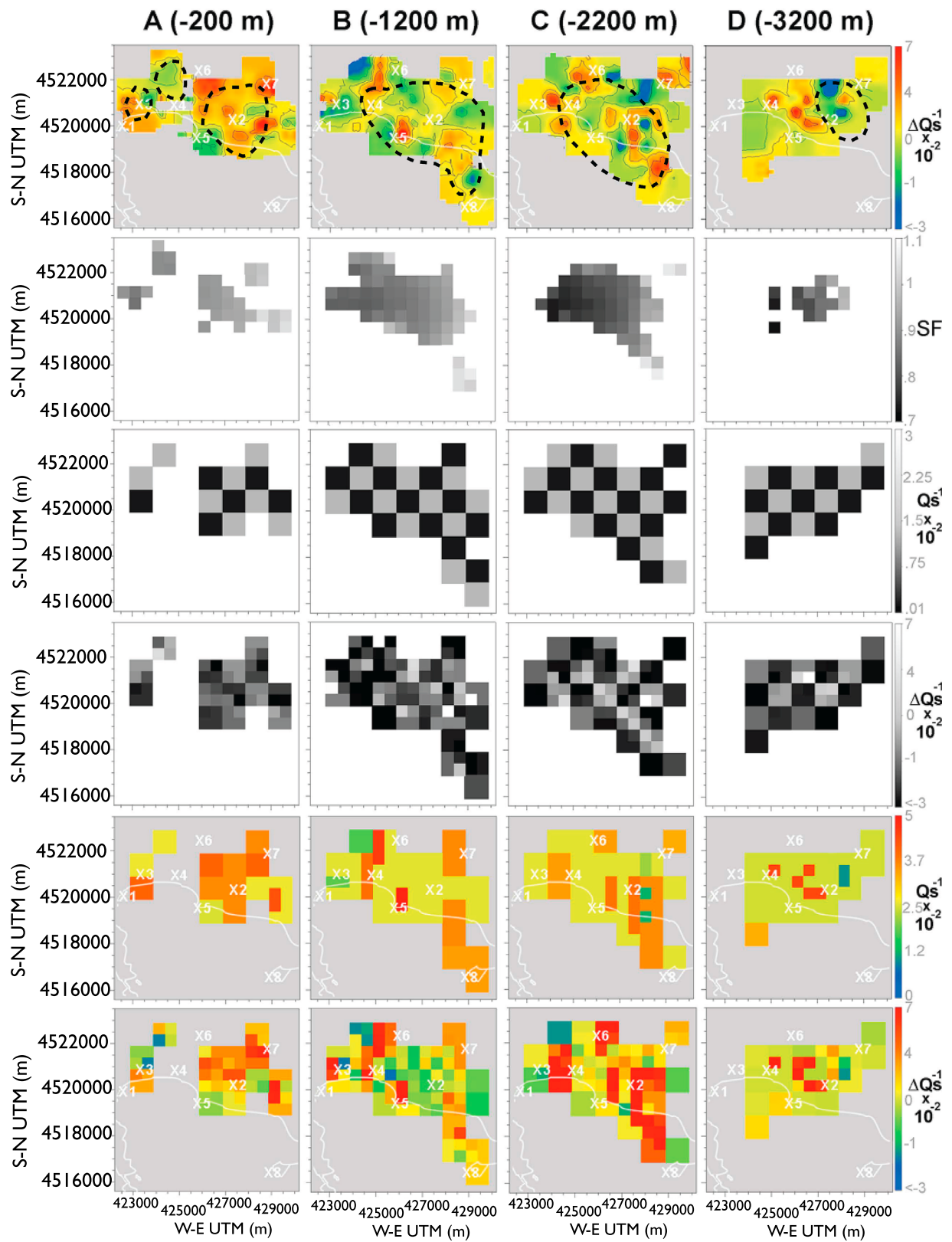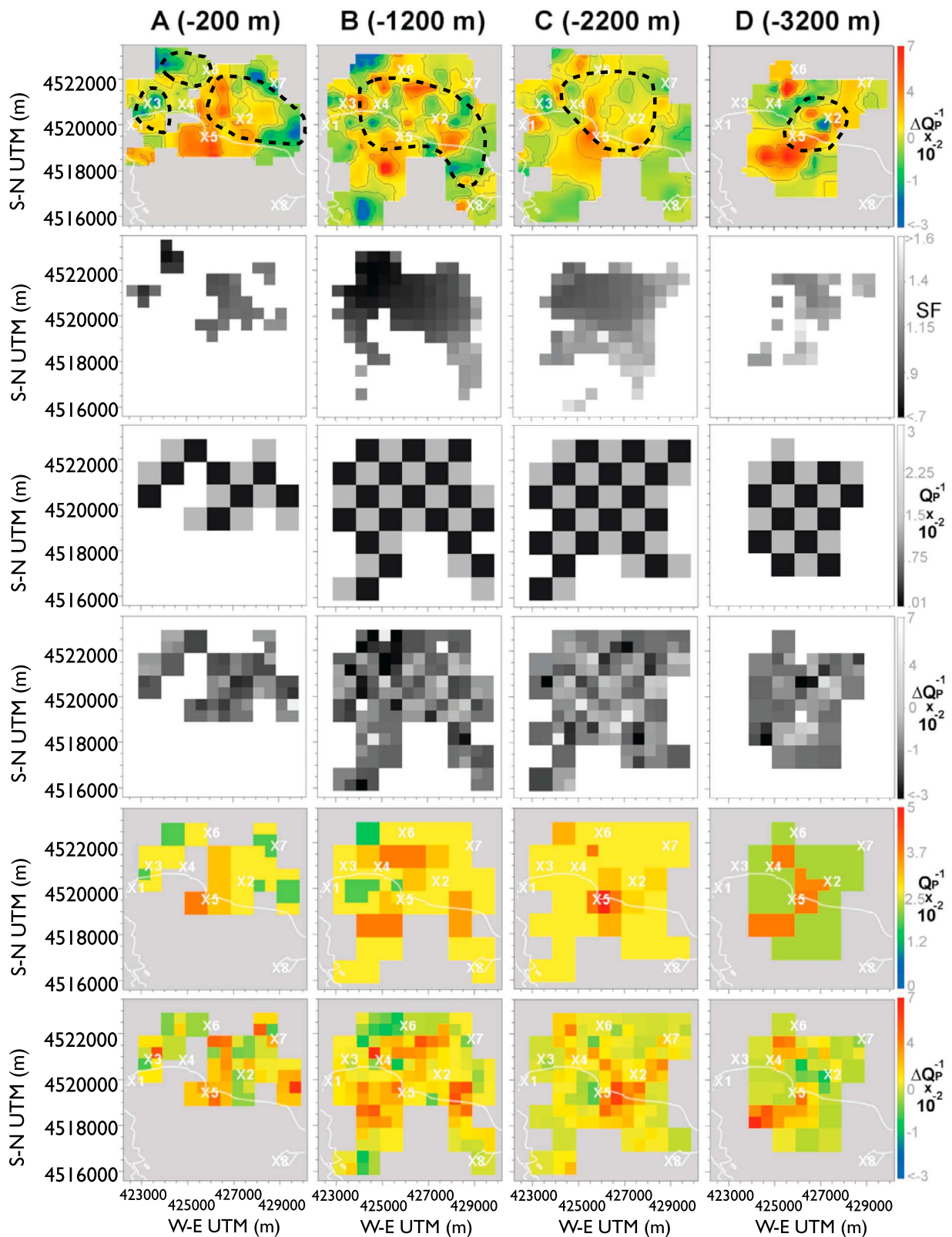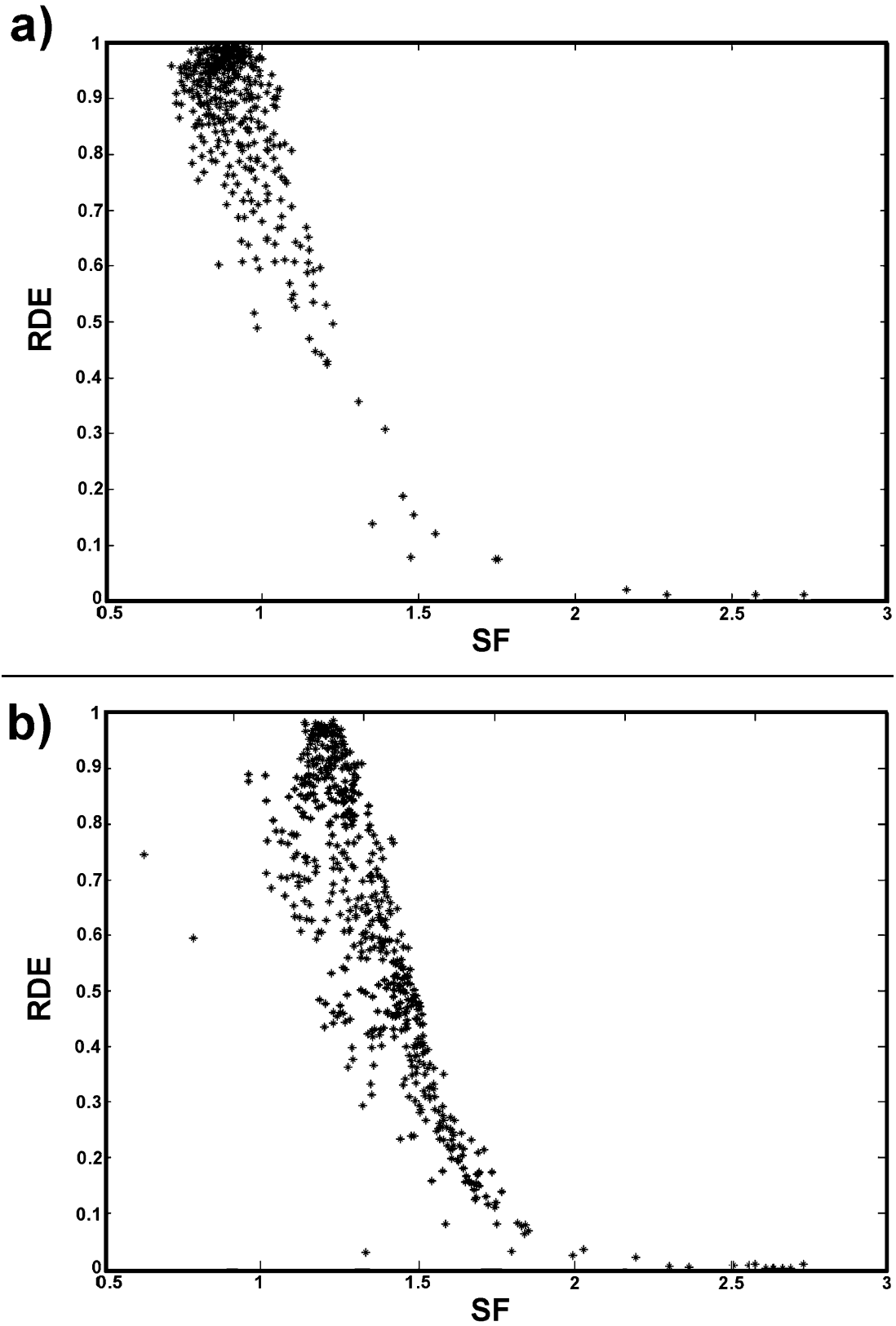
Figure 3

Figure 4. As for Figure 3, for P-waves.

volumes located in the north-western and central parts of the caldera, in the depth range of −500 to −2500 m.

[15] The effects of smearing on the solution can be seen on the checkerboard test, performed by imposing an a priori

S-wave (Figure 3, third row) and P-wave (Figure 4, third row) attenuation structure to the area. As already highlighted in other studies [*Koulakov*, 2009], assuming an input checker-board structure at the maximum resolution (in the present

Figure 5. Plots of the diagonal element of the resolution matrix (RDE) versus the spread function (SF) values for (a) the Q_S^{-1} model and (b) the Q_P^{-1} model.

case, 500 m) produces an underestimation of the smearing effects. Thus, we assume as input a checkerboard structure done with 1000 *m* side blocks (Figure 3, third row). We generate the synthetic spectral ratios of equation (2) and add to these values a Gaussian random error with zero mean and 3 sigma equal to the 20% of the data value. Finally, we solve the inversion for these synthetic data using the CN method. The checkerboard test output (Figure 3, fourth row) shows a good agreement with the input in the center of the caldera (Solfatara, Mt. Nuovo, La Starza and Pozzuoli); smearing effects are visible in the images at shallower depth (Figure 3a) between Pozzuoli and La Starza. Some smearing is seen in the areas of Mofete and Mt. Nuovo (Figure 3b, X1 and X3) at −1200 m (Figure 3b), as well as in the Agnano area (Figure 3b, X7). The best resolved S-wave anomalies are located around −2200 m (Figure 3c), in the whole area under study. The resolution of 1000 m is the highest available at −3200 m (Figure 3d). This test confirms that the maximum S-wave resolution can be effectively obtained in the inner volume of the caldera, between 0 m and −3500 m. Outside of this region, the images need to be interpreted with caution, due to partial distortion of the solution. The checkerboard test for P-waves was performed using the SD method to obtain the synthetic data vector (Figure 4, third and fourth rows), and solving a wider number of blocks. In the center of the caldera, even though the intensity of the anomalies is considerably damped, the checkerboard structure is still recognizable in the −200 and −1200 images. Part of the bay, south of the city of Pozzuoli (Figure 4, X5) shows a small smearing effect in this depth range. The image at −2200 m shows a poor reconstruction of the anomalies under Mt. Nuovo and La Starza (Figure 4, X3 and X4), while the volumes under Solfatara, Pozzuoli and north of Nisida (Figure 4, X2, X5 and X8) are well resolved. As in the case of the S-waves, a resolution of 1000 m is the highest available at −3200 m (Figure 4d).

[16] The final test is performed following the approach of *Schurr et al.* [2003], using as input a characteristic model (a simplified version of the data inversion) to check the output size and the intensity of the anomalies (Figure 3 and Figure 4, fifth rows, for S-waves and P-waves, respectively). The reason for this test, together with the commonly adopted checkerboard test, is that we wish to explore the true resolving capability in the zone of maximum interest. The error added to the data is the same as that applied in the checkerboard tests. The outputs of the tests are shown in Figure 3 and Figure 4, sixth rows, for ΔQ_S^{-1} and ΔQ_P^{-1}, respectively. The S-wave image at shallower depth (Figure 3a) shows the good reconstruction of the anomalies in the whole slice. In contrast, the output of the test for P-waves at the same depth does not reproduce well the eastern part of input images (Figure 4a). The S-image at −1200 m (Figure 3b) highlights the presence of a ghost high-attenuation image in the area of Mofete (Figure 3, X1), probably due to the strong smearing of the nearby high-attenuation zones. The P-image at −1200 m (Figure 4b) shows a very good agreement between input and output, confirming that, in this depth range, the P-wave attenuation parameters are relatively resolved. The only non-resolved anomaly (for the P image) is the low attenuation zone under Mofete (Figure 4b, X1). The same happens for the S-wave synthetic test. In the depth range between −1500 and −2500 the input image is fairly well resolved for both
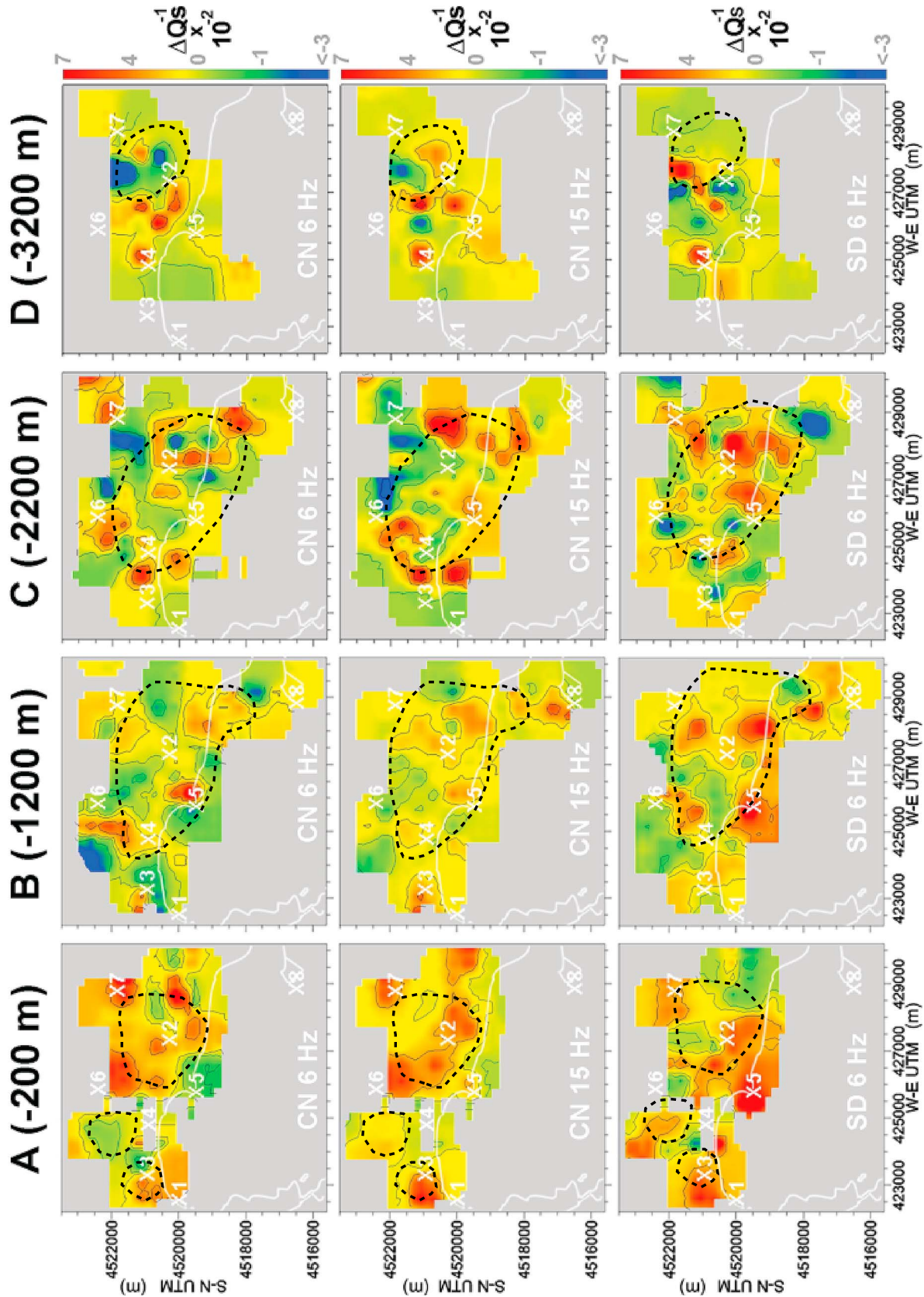
S-waves and P- waves (Figure 3c and Figure 4c). The S-wave images at −3200 m are relatively well reproduced (Figure 3d); the contrary occurs for P-waves (Figure 4d) in the center of the caldera, between Solfatara and Pozzuoli (Figure 4d, X2 and X5). The 'characteristic' test indicates where the interpretation can be carried out in terms of physical quantities or lithology.
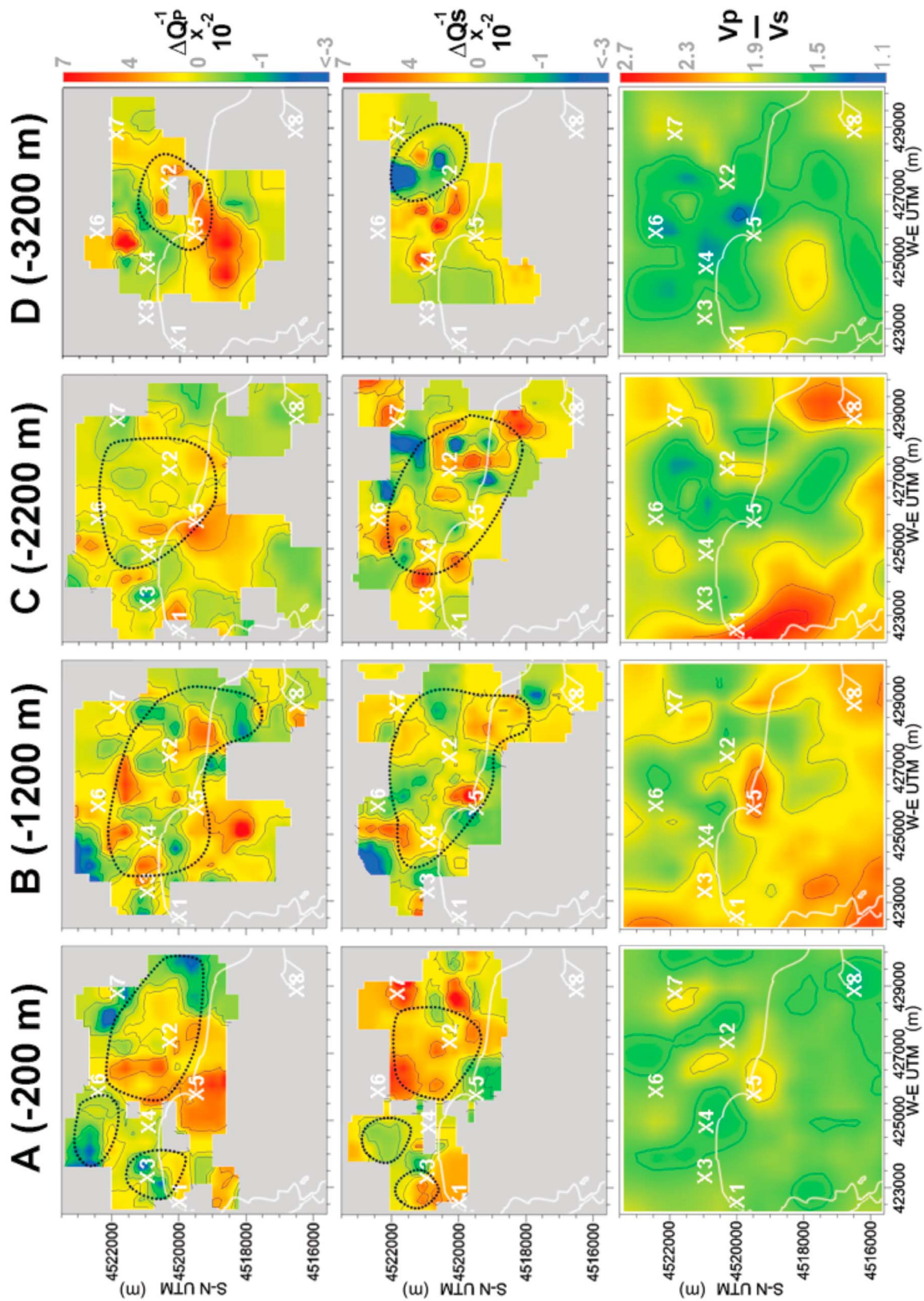
7. Results

[17] The results are shown in the horizontal slices of Figure 6 and Figure 7, crossing the volume under study at −200 m, −1200 m, −2200 m and −3200 m, and on the vertical sections of Figure 8. These are drawn on the basis of a compromise between the maximum resolution achievable and the presence of volcanological features; the unresolved cells as well as the zones whose unreliability was shown by synthetic tests are in grey. The black dashed lines in Figure 7 contour the maximum resolution cells, drawn using the results of the checkerboard tests. In Figure 8 the numbered dashed rectangles highlight the main features that will be discussed and interpreted in the following. The images obtained in two frequency bands centered respectively at 6 Hz (Figure 6, first row) and 15 Hz (Figure 6, second row) are shown together with the results of the S-wave attenuation imaging obtained at 6 Hz with the SD method (Figure 6, third row), in the four horizontal panels at increasing depth. The images at $f_C = 15$ Hz better reflect the small-scale structures than those centered at 6 Hz, due to the shorter wavelengths. Within the limits of our resolution, we cannot find significant strong differences between the images at the different frequencies in the resolved volumes obtained through the synthetic test. Just some small differences can be observed at the borders of the images, where the amount of smearing is stronger, e.g., in the northwestern part of Figure 6a, north of Mt. Nuovo and La Starza (Figure 6, X3 and X4), where the attenuation features look opposite. Consequently, we compared the only attenuation image obtained in the band centered at 6 Hz with the velocity images. The unique macroscopic differences between the images obtained with CN and SD methods for S-waves are visible in the tomograms at −200 m (Figure 6a) under the city of Pozzuoli (compare first and third rows of Figure 6). At this depth the CN method shows a strong lateral contrast, approximately separating the land from the sea along the coastline, while SD shows in the same area a strong high-attenuation anomaly. This difference might be due to anomalous behavior of the W11 station (Figure 1c) transfer function (not reported in the data sheets of the 1983–1984 seismic survey, D. Galluzzo, personal communication, 2009) and might have affected the SD method. The CN method would remain unaffected by this effect due to the CN procedure.

8. Joint Interpretation of the Velocity and Attenuation Images

[18] We have based the interpretation of our findings on the analysis of the main features of the attenuation images, isolating the volumes characterized by strong laterally and/or in-depth contrasts. Then, we have associated these volumes with those corresponding to all of the other available V_P/V_S, V_P or V_S images. Finally, interpretations were constrained by

Figure 6. As for Figure 3, with the Q_S^{-1} tomography results obtained at 6 Hz (top row) and 15 Hz (middle row) with the CN method, and at 6 Hz with the SD method (bottom row). The common color scale represents the variations from the average S-wave inverse quality factor. The bold black dashed lines roughly contour the maximum resolution areas (500 m).

Figure 7. As for Figure 2, with the results of the P-wave (top row) and S-wave (middle row) attenuation tomography. The quantity represented is the variation respect to the average quality factor. The V_P/V_S ratio (bottom row) is deduced by the measures of absolute velocity of *Battaglia et al.* [2008]. The bold black dashed lines roughly contour the maximum resolution areas (500 m).
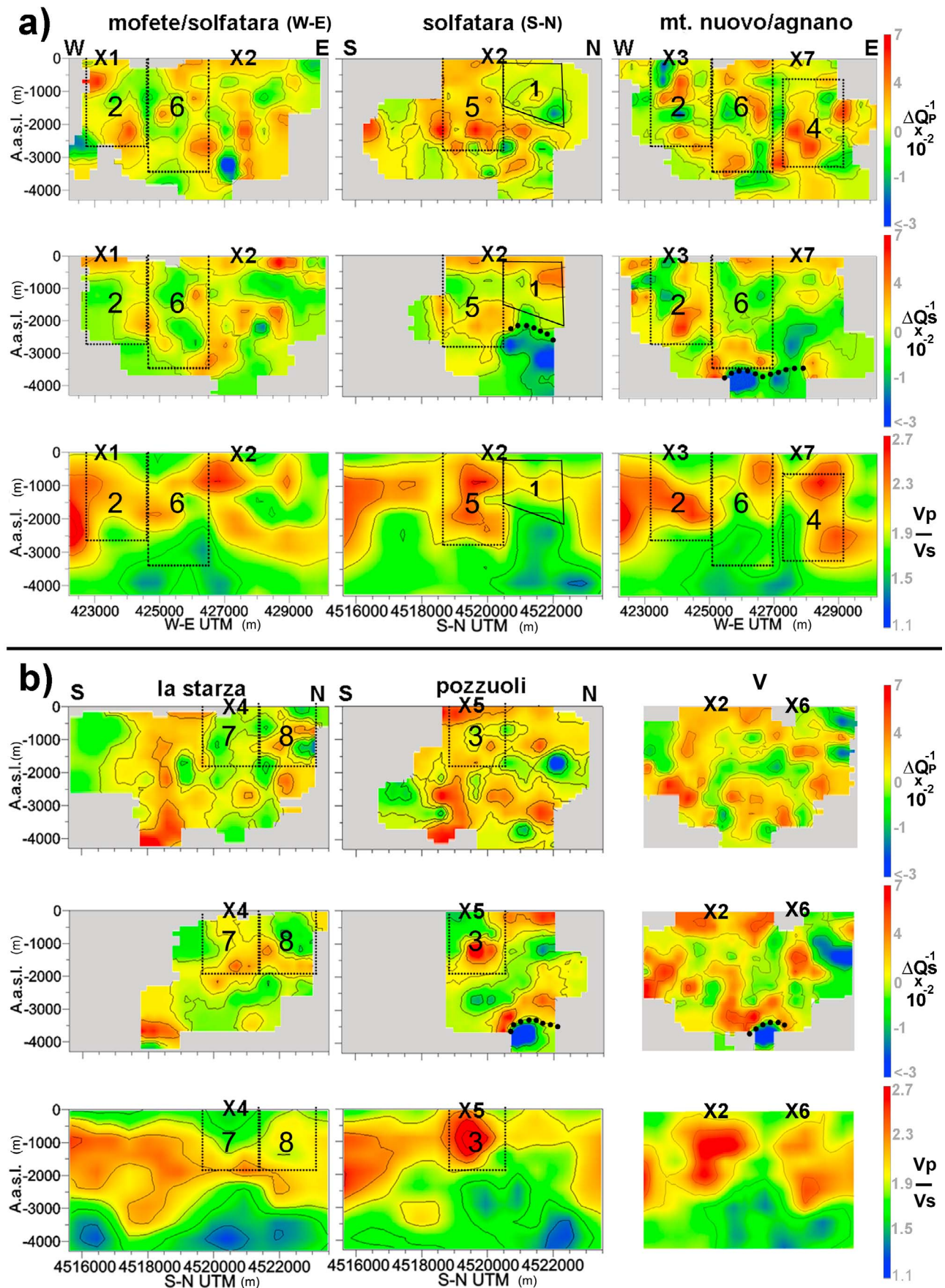
Figure 8

the numerous seismological, geological, volcanological and geochemical evidence available in the area.

8.1. Hydrothermal Basins Under Pozzuoli, Mofete-Mt. Nuovo, and Agnano

[19] The V_P/V_S images in Figure 7b show a maximum of the V_P/V_S ratio corresponding to high Q_P^{-1} and Q_S^{-1} in the center of the caldera, prevalently under the city of Pozzuoli (Figure 7, X5). Looking at the "pozzuoli" panels (Figure 8b, "pozzuoli", dashed rectangle (DR) number 3), a very high V_P/V_S ratio ($V_P/V_S = 2.6$) matches well the high-attenuation anomaly located under Pozzuoli, between 0 and −2000 m. The Q_S^{-1} pattern obtained is compatible with the presence of a hydrothermal basin under the city of Pozzuoli, confirming the results of [*Vanorio et al.*, 2005]. High-attenuation patches for both P-waves and S-waves are clearly visible between the surface and −3000 m, according to our vertical resolution, for the volumes under Mofete and Mt. Nuovo (Figures 7a–7c, X1 and X3, and Figure 8a "mofete/solfatara (W-E)" and "mt. nuovo", DR 2). The high V_P/V_S ratio between 0 m and −3000 m is in good agreement with the high Q_P^{-1} and Q_S^{-1} in the attenuation tomograms. We interpret these vertical high-attenuation volumes as a pathway of H_2O (high temperature vapors) and CO_2 up to the surface, towards the area surrounding Mt. Nuovo. *Todesco et al.* [2003] recognized two aquifers in the Mofete area, with good lateral continuity: a shallow one between −150 *m* and −300 *m*, with temperatures between 100 and 130°C, and a deeper one between −1250 *m* and −1600 *m*, with a temperature of 300°C. Their positions closely match the high Q_S^{-1} volumes in Figure 8a, "mofete/solfatara (W-E)", DR 2. Finally, the high Q_P^{-1} zones located under Agnano, between 0 m and −3500 m (Figure 8a, the eastern part of panels "mt. nuovo/agnano", DR 4) show good correlation with the high V_P/V_S. A relevant aquifer with temperatures of the order of 250°C has been described in different studies below the Agnano Plain at −1400 m in different studies [see *Todesco et al.*, 2003, and references therein]. This area of high attenuation is connected with the high attenuation anomaly in the center of the caldera (Figure 7d).

8.2. Solfatara

[20] In Figure 8a, "solfatara (S-N)", there is an anomalous low Q_P^{-1} located prevalently North of the Solfatara benchmark (X2) and indicated in the corresponding tomogram by the polygon marked by number 1, which affects at least the volumes between 0 m and −2500 m. *De Lorenzo et al.* [2001] revealed in the same area a volume characterized by high Q_P^{-1} at a lower resolution, with a completely different approach to the estimation of the seismic signatures. North of Solfatara, V_P/V_S is generally lower than in the other directions, while the Q_S^{-1} is generally high. The region is characterized by high temperature rocks at shallow depths, and by conductive heat transfer, as inferred by measurements in geothermal wells [*Todesco et al.*, 2003]. The high Q_S^{-1} and low Q_P^{-1} patches,

together with the low V_P/V_S ratio and the generally low V_P (as highlighted looking at the images of *Battaglia et al.* [2008]), are compatible with the presence of a small reservoir of gas (CO_2) [*Hansen et al.*, 2004]. This interpretation is supported by the evidence of many fumaroles at the surface [*Caliro et al.*, 2007], which have been interpreted by *Todesco et al.* [2003] as due to the escape of fluids from a magma chamber towards geothermal reservoirs, and from there to the surface. The south-western parts of the Solfatara is characterized by high Q_P^{-1}, high Q_S^{-1}, and high V_P/V_S, at least between 0 and −3000 m, as expected for a strongly fractured medium permeated by fluids (see, e.g., Figure 8a, "mofete/solfatara (W-E)", SD 5), probably connected to the Pozzuoli hydrothermal basin.

8.3. Attenuation Materials Near the Zone of Maximum Uplift: La Starza Fault

[21] In the western part of the attenuation tomograms of Figures 7b and 7c, the high Q_P^{-1} and high Q_S^{-1} zones of Mofete-Mt. Nuovo and Pozzuoli (Figure 6, X1, X3 and X5) are separated by an approximately SW-NE oriented low Q_P^{-1} and low Q_S^{-1} structure. This low-attenuation volume is characterized by low V_P/V_S. In Figure 8a, "mofete/solfatara (W-E)" and "mt. nuovo/agnano" (DR 6), this almost vertical low Q_P^{-1} and low Q_S^{-1} structure is clearly evident, between −500 and −4000 m. The low Q_P^{-1} values strictly correlate with the low Q_S^{-1} and low V_P/V_S values. This zone suffered the maximum surface uplift in the 1983–1984 bradyseismic crisis, and is characterized by strong vertical contrast between the SW-NE low-attenuation structure described above and the high-attenuation materials underneath Pozzuoli-Solfatara. The La Starza fault (Figure 7b, X4) is clearly depicted by one of this Q_S^{-1} contrasts, between 0 and −2500 m (see also Figure 8b, "la starza", DR 7). The same tomograms (DR 8) show the presence of high Q_S^{-1}, and high V_P/V_S in the northern part, in correspondence with the presence of fumaroles at the surface [*Di Vito et al.*, 1999], suggesting the presence of a hard rock medium filled with fluids and gasses, connected with the hydrothermal basin under the Mofete-Mt. Nuovo area and to the gas reservoirs under the northern part of Solfatara.

8.4. High-Attenuation Volumes at −2200 m

[22] The attenuation and velocity features at −2200 m are shown in Figure 7c. These tomograms show hard rock volumes (characterized by low attenuation), surrounding a heterogeneous high attenuation structure, with its center located among La Starza, Pozzuoli and Solfatara (Figure 7c, X4, X5 and X2). The low V_P/V_S ratio (lower than 1.5) in the center of this low velocity and high-attenuation structure indicates the absence of melt in the center of the area under study, as recently highlighted by *Vanorio et al.* [2005]. Two zones of high Q_P^{-1}, high Q_S^{-1}, and high V_P/V_S are visible at this depth: the first is situated between Mt. Nuovo and San Vito (Figure 7c, northwestern part, X3 and X6), and intersects the

Figure 8. The same as for Figure 6 for six vertical WE and SN sections, crossing the Campi Flegrei caldera. The columns are labeled with the name of the area crossed by the section and with the marker highlighting the area of volcanological interest. The black polygon marked by number 1 in panel "solfatara (S-N)" shows an area of low Q_P^{-1}, high Q_S^{-1} and generally lower V_P/V_S (see main text). The dashed numbered rectangles contour the volumes where interesting correlations between velocity and attenuation were found and discussed in the text. Column V shows the tomograms for a vertical section crossing the Campi Flegrei caldera diagonally. The V_P/V_S ratio was deduced by the measures of absolute velocity of *Battaglia et al.* [2008].

area of La Starza (Figure 7c, X4); the second is located beneath the eastern part of Solfatara (Figure 7c, south-eastern part, X2). We can interpret these regions as zones where the presence of melt is possible, in agreement with previous volcanological interpretations [*D'Antonio et al.*, 1999]. A third zone of high Q_P^{-1}, high Q_S^{-1} and low V_P/V_S is located beneath Pozzuoli (the high Q_P^{-1} area extends towards the bay). Despite the lower resolution, it is quite reasonable that this anomaly is the top of a wider anomaly located beneath, as described in the next section.
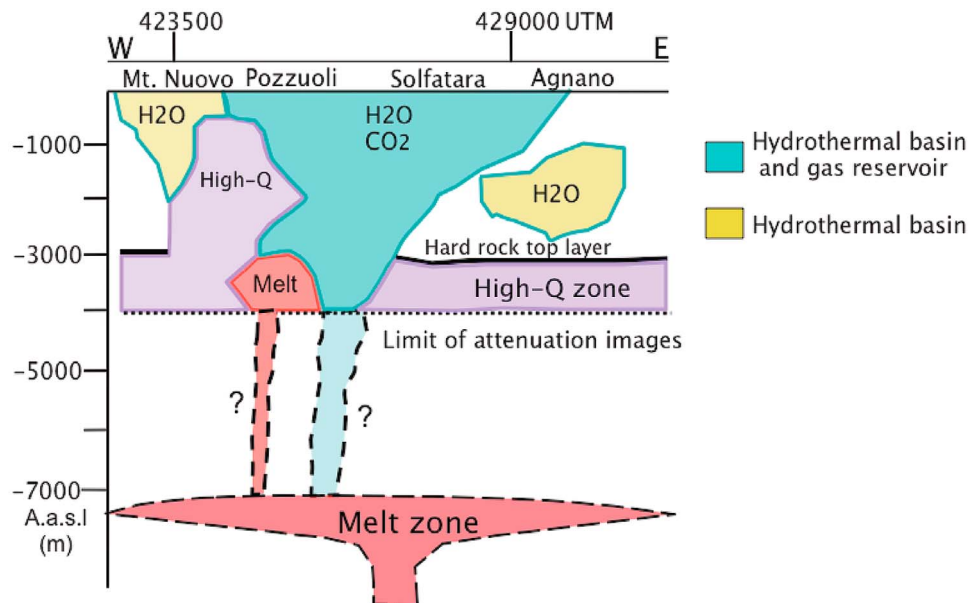
8.5. Materials Under −3000 m

[23] *Zollo et al.* [2008] recently observed a seismic interface located −2700 m under the Campi Flegrei caldera, using seismic reflection analysis. The sharp increment in both V_P and V_S at this depth was also seen in the velocity tomograms of *Battaglia et al.* [2008]. It matches well the S-wave attenuation contrast observed in a wide area north and east of the center of the caldera (see in particular the bold dashed black line in Figures 8a and 8b, "solfatara (S-N)", "mt. nuovo/ agnano", "pozzuoli" and "V"). The attenuation and V_P/V_S tomograms under −3000 m are discussed in Figure 7d. The V_P/V_S ratio is generally low in the center of the image. The Q_S^{-1} tomogram roughly shows low-attenuation materials, except for a large high S-wave attenuation anomaly extending beneath La Starza, Pozzuoli and Solfatara (Figure 7d, X4, X5 and X2), possibly connected with an average attenuation area in the south-western corner of the image. The same attenuation pattern is recognizable in the Q_P^{-1} tomogram. While the northeastern part of the image is characterized by low attenuation, the central and south-western parts of the tomograms have high attenuation. The south-western high-attenuation anomaly shows very good correlation with a high V_P/V_S area in the same depth range. To the limits of our resolution, this seismological evidence suggests the presence of melt or highly cracked rigid materials in this area. The attenuation pattern at this depth could also indicate the presence of small magma patches in the area of Pozzuoli (Figure 7d, X5), even though the low V_P/V_S would not suggest a large magma batch.

9. Concluding Remarks

[24] The top of a laterally extended low P-wave and S-wave attenuation zone is present around −3000 m, in agreement with the discontinuity described by *Zollo et al.* [2008] using seismic reflection techniques, and observed by *Battaglia et al.* [2008] using seismic velocity tomography. Magnetotelluric surveys *Zollo et al.* [2006] have shown a low resistivity zone, 4000 m under the town of Pozzuoli, while V_P/V_S ratio tomography in the same area has been interpreted using the experimental measurements of the physical properties of the rock from Campi Flegrei samples as a constraint to evidence an horizontal interface around this depth. This laterally extended discontinuity appears to be laterally uniform, in the attenuation images, but includes visible high Q_P^{-1} and high Q_S^{-1} anomalies in its central part. Anyway, the low V_P/V_S ratio value at 4000 m in depth is not consistent with the presence of magma or fluids [*Vanorio et al.*, 2005]. We interpret the high attenuation and low V_P/V_S anomalies located beneath La Starza and Pozzuoli-Solfatara around −3000 m as due to the presence of a vapor-filled conduit, a

pathway for the magmatic gas flow that is detected at the surface [*Caliro et al.*, 2007]. *Nakajima and Hasegawa* [2003] showed that a narrow conduit with low V_P and low V_S in the upper crust beneath the Naruko volcano does not have a high V_P/V_S value. Similar low-velocity ratio conduits have been reported in Redoubt volcano, Alaska [*Benz et al.*, 1996], Mt. Etna, Italy [*Villaseñor et al.*, 1998], Aso volcano, Japan [*Sudo and Kong*, 2001], and Mt. Vesuvius [*Scarpa et al.*, 2002] and they have been interpreted as highly fractured zones and/or active magma conduit systems. Low V_P/V_S anomalies have also been detected in geo- and hydro-thermally active areas, such as the Yellowstone caldera [*Chatterjee et al.*, 1985], the Coso Region [*Walck*, 1988] and the Geysers geothermal area [*Julian et al.*, 1996], California. In Campi Flegrei, the velocity anomalies inside the areas of strong attenuation at −3200 m can be explained by the presence of the vapor phase in the rock matrix, on the basis of the theory of *Takei* [2002]. Experimental evidence suggests that the hot vapor phase has a dominant role in causing low V_P/V_S anomalies in Campi Flegrei, since the thermal activity in this area is very high. Indeed, it is likely that vapor-filled fracture zones or volcanic deposits are distributed inside the caldera, although not exactly in its center. These small melt patches, which might be present in the high Q_P^{-1}, high Q_S^{-1} volumes imaged under −2000 m by the present tomography, might contribute to the magmatic gas flow, and might also interact with the hydrothermal basins and gas reservoirs recognized at shallower depths. A 7500 m deep, 1000 m thick low velocity layer (well outside the volumes under study here) has been revealed by *Zollo et al.* [2008], and has been interpreted as being associated with a mid-crust, partial melting zone beneath the caldera, which suggests that a large magmatic sill is present well within the basement formation. When constrained by this result, the joint interpretation of the velocity and attenuation features lead us to the final concept that the attenuation anomaly around −3200 m (in the central part of the tomograms in Figure 7d) constitutes the upper part of a vapor-filled conduit. This conduit may be connected with the sill at −7500 m and/or associated with the melt zone located at −3200 m in the south-western part of the tomograms in Figure 7d, and may contribute to the transport of magmatic gases towards the surface, as schematically proposed by *Nakajima and Hasegawa* [2003] for the Naruko volcano.

[25] The present attenuation tomography is also a strong clue for the presence of three geothermal basins, located beneath Pozzuoli, between 0 m and −3000 m, beneath Mofete and Mt. Nuovo, between −500 m and −2500 m, and beneath Agnano, between −1000 m and −3000 m. Geothermal drilling has shown high-temperature gradients in all of this area (150°C km^{-1}), and the presence of two distinct aquifers in the Agnano area (150–300 m and 1250–1600 m in depth). These aquifers should interact with this conduit, favoring the upward circulation of hot non-magmatic vapor that constitute the main part of the fumarole gases at the surface [*Caliro et al.*, 2007]. The evidence of a low Q_P^{-1} volume north-eastward of the Solfatara crater is also compatible with the presence of a gas reservoir between 0 and −2500 m, following the interpretative scheme of *Hansen et al.* [2004], and confirmed by the interpretations of *Todesco et al.* [2003] and [*Caliro et al.*, 2007] on the basis of observations of diffuse degassing. Finally, attenuation tomography images the maximum uplift zone during the 1983–1984 bradyseismic crisis as

Figure 9. Schematic illustration of the uppermost crust crossing Campi Flegrei from West to East. This depicts the interpretation based essentially on the results of the present study on attenuation tomography compared with those from velocity. As explained in the text, the interpretation is carried out with reference to the methodology reported by *Hansen et al.* [2004], and summarizes the present study together with many other interpretations of the geological structure of Campi Flegrei. In particular the melt zone at −7500 m and the high Q zone at −3000 m were deduced by *Zollo et al.* [2008].

a zone of strong P-wave and S-wave attenuation contrast; in particular, the zone of high seismicity during this 1983–1984 seismic sequence is practically coincident with the "La Starza" structure [*Di Vito et al.*, 1999], which is depicted by this contrast.

[26] A schematic sketch of our interpretation is shown in Figure 9, where we summarize in a qualitative color image the main features of the attenuation image obtained in the present study, together with information derived from active and passive velocity tomography. Interestingly our method evidences a possible small melt volume just below the maximum uplift area of the 1983–1984 bradyseismic crisis. Velocity tomography studies did not show clear evidence of extensive melting zones between 0 and −5500 m; however, magma intrusions and the migration of fluids with an increase in pressure into a hydrothermal reservoir, with a consequent increase in pressure, have been considered as a reasonable source for the strong ground deformations that have occurred in the area [*Bonafede and Mazzanti*, 1998; *Gaeta et al.*, 1998; *Gottsman et al.*, 2006; *Battaglia et al.*, 2006]. It is important to conclude with the note that all of the attenuation images in this study were obtained with passive data recorded over a small time interval during the 1983–1984 crisis. The comparisons are instead carried out using images obtained from a data set spanning a larger time interval. Consequently, possible changes in the geological structure, such as those revealed at Mt. Etna [*Patanè et al.*, 2006], due to the ongoing dynamics of Campi Flegrei [see *Saccorotti et al.*, 2007, and references therein] cannot be imaged.

References

Abercrombie, R. E. (1995), Earthquake source scaling relationships from −1 to 5 M_L using seismograms recorded at 2.5-km depth, *J. Geophys. Res.*, *100*, 24,015–24,036.

Aki, K. (1980), Attenuation of shear-waves in the lithosphere for frequencies from 0.05 to 25 Hz, *Phys. Earth Planet. Inter.*, *21*, 50–60.

Aster, R. C., and R. P. Meyer (1988), Three-dimensional velocity structure and hypocenter distribution in Campi Flegrei caldera, Italy, *Tectonophysics*, *149*, 195–218.

Aster, R. C., and R. P. Meyer (1989), Determination of shear and compressional wave velocity variations and hypocenter locations in a rapidly inflating caldera: The Campi Flegrei, *Phys. Earth Planet. Intet.*, *55*, 313–325.

Aster, R. C., B. Borchers, and C. Thurber (2005), *Parameter Estimation and Inverse Problems*, 1st ed., vol. 90, 320 pp., Elsevier Acad., New York.

Anderson, J. G., and S. E. Hough (1984), A model for the shape of the Fourier spectrum of accelleration at high frequecies, *Bull. Seismol. Soc. Am.*, *74*, 1969–1993.

Bai, C., and S. Greenhalgh (2005), 3D multi-step travel time tomography: imaging the local, deep velocity structure of Rabaul volcano, Papua New Guinea, *Phys. Earth Planet. Inter.*, *15*, 259–275.

Battaglia, J., C. Troise, F. Obrizzo, F. Pingue, and G. De Natale (2006), Evidence of fluid migration as the source of deformation at Campi Flegrei caldera (Italy), *Geophys. Res. Lett.*, *33*, L01307, doi:10.1029/2005GL024904.

Battaglia, J., A. Zollo, J. Virieux, and D. Dello Iacono (2008), Merging active and passive data sets in traveltime tomography: The case study of Campi Flegrei caldera (southern Italy), *Geophys. Prospect.*, *56*, 555–573.

Benz, H. M., B. A. Chouet, P. B. Dawson, J. C. Lahr, R. A. Page, and J. A. Hole (1996), Three-dimensional P and S wave velocity structure of Redoubt Volcano, Alaska, *J. Geophys. Res.*, *101*, 8111–8128.

Berrino, G., G. Corrado, G. Luongo, and B. Toro (1984), Ground deformation and gravity changes accompanying the 1982 Pozzuoli uplift, *Bull. Volcanol.*, 47, 187–200.

Block, L. V. (1991), Joint hypocenter-velocity inversion of local earthquakes arrival time data in two geothermal regions, Ph.D. thesis, Mass. Inst. of Technol., Cambridge.

Boatwright, J. (1980), A spectral theory fo circular seismic sources: Simple estimates of source dimension, dynamic stress drop and radiated energy, *Bull. Seismol. Soc. Am.*, 70, 1–27.

Bonafede, M., and M. Mazzanti (1998), Modeling gravity variations consistent with ground deformation in the Campi Flegrei caldera, Italy, *J. Volcanol. Geotherm. Res.*, 81, 137–157.

Caliro, S., G. Chiodini, R. Moretti, R. Avino, D. Granieri, M. Russo, and J. Fiebig (2007), The origin of the fumaroles of La Solfatara (Campi Flegri, South Italy), *Geochim. Cosmochim. Acta*, 71, 3040–3055.

Chatterjee, S. N., A. M. Pitt, and H. M. Iyer (1985), Vp/Vs ratios in the Yellowstone National Park region, Wyoming, *J. Volcanol. Geotherm. Res.*, 26, 213–230.

Chouet, B. (1996), New methods and future trends in seismological volcano monitoring, in *Monitoring and Mitigation of Volcano Hazards*, edited by R. Scarpa and R. I. Tilling, pp. 23–97, Springer, Berlin.

Chouet, B. (2003), *Volcano Seismol.*, *Pure Appl. Geophys.*, 160, 739–788.

Corrado, G., I. Guerra, A. Lo Bascio, G. Luongo, and R. Rampoldi (1976), Inflation and microearthquake activity at Phlegrean Fields, Italy, *Bull. Volcanol.*, 40, 1–20.

D'Antonio, M., I. Civetta, G. Orsi, L. Pappalardo, M. Piochi, A. Carandente, S. de Vita, M. A. Di Vito, and R. Isaia (1999), The present state of the magmatic system of the Campi Flegrei caldera based on a reconstruction of its behavior in the past 12 ka, *J. Volcanol. Geotherm. Res.*, 91, 247–268.

De Gori, P., C. Chiarabba, and D. Patanè (2005), *Qp* structure of Mount Etna: Constraints for the physics of the plumbing system, *J. Geophys. Res.*, 110, B05303, doi:10.1029/2003JB002875.

De Lorenzo, S., A. Zollo, and F. Mongelli (2001), Source parameters and three-dimensional attenuation structure from the inversion of micro-earthquake pulse width data: Q_P imaging and inferences on the termal state of Campi Flegrei caldera (southern Italy), *J. Geophys.Res.*, 106, 16,265–16,286.

Del Pezzo, E., S. De Martino, and M. T. Parriniello (1993), Seismic site amplification factors in Campi Flegrei, southern Italy, *Phys. Earth Planet. Inter.*, 78, 105–117.

Del Pezzo, E., F. Bianco, L. De Siena, and A. Zollo (2006a), Small scale shallow attenuation structure at Mt. Vesuvius, Italy, *Phys. Earth Planet. Inter.*, 157, 257–268.

Del Pezzo, E., F. Bianco, and L. Zaccarelli (2006b), Separation of Qi and Qs from passive data at Mt. Vesuvius: A reappraisal of the seismic attenuation estimates, *Phys. Earth Planet. Inter.*, 159, 202–212.

De Natale, G., G. Iannaccone, M. Martini, and A. Zollo (1987), Seismic sources and attenuation properties at the Campi Flegrei volcanic area, *Pure Appl. Geophys.*, 125(6), 883–917.

De Siena, L., E. Del Pezzo, F. Bianco, and A. Tramelli (2009), Multiple resolution seismic attenuation imaging at Mt. Vesuvius, *Phys. Earth Planet. Inter.*, 173, 17–32.

Dias, N. A., L. Matias, N. Louren ço, J. Madeira, F. Carrilho, and J. L. Gaspar (2007), Crustal seismic velocity structure near Faial and Pico Islands (AZORES), from local earthquake tomography, *Tectonophysics*, 445, 301–317.

Di Renzo, V., M. A. Di Vito, I. Arienzo, A. Carandente, L. Civetta, M. D'Antonio, F. Giordano, G. Orsi, and S. Tonarini (2007), Magmatic history of Somma-Vesuvius on the basis of new geochemical and isotopic data from a deep borehole (Camaldoli dellaTorre), *J. Petrol.*, 48, 753–784.

Di Vito, M. A., L. Lirer, G. Mastrolorenzo, and G. Rolandi (1987), The Monte Nuovo eruption (Campi Flegrei, Italy), *Bull. Volcanol.*, 49, 608–615.

Di Vito, M. A., R. Isaia, G. Orsi, J. Southon, S. de Vita, M. D'Antonio, M. Pappalardo, and L. M. Piochia (1999), Volcanism and deformation since 12,000 years at the Campi Flegrei caldera (Italy), *J. Volcanol. Geotherm. Res.*, 91, 221–246.

Eberhart-Phillips, D., M. Reyners, M. Chadwick, and J. M. Chiu (2005), Crustal heterogeneity and subduction processes: 3-D V_P, V_P/V_S and Q in the southern North Island, New Zealand, *Geophys. J. Int.*, 162, 270–288.

Gaeta, S. G., G. De Natale, F. Peluso, G. Mastrolorenzo, D. Castagnolo, C. Troise, F. Pingue, G. Mita, and S. Rossano (1998), Genesis and evolution of unrest episodes at Campi Flegrei caldera: The role of thermal fluid-dynamical processes in the geothermal system, *J. Geophys. Res.*, 103, 20,921–20,933.

Gottsman, J., H. Rymer, and G. Berrino (2006), Unrest at the Campi Flegrei caldera (Italy): A critical evaluation of source parameters from geodetic data inversion, *J. Volcanol. Geotherm. Res.*, 150, 132–145.

Gusev, A. A., and I. R. Abubakirov (1999), Vertical profile of effective turbidity reconstructed from broadening of incoherent body-wave pulses, *Geophys. J. Int.*, 136, 309–323.

Hansen, S., C. H. Thurber, M. Mandernach, F. Haslinger, and C. Doran (2004), Seismic velocity and attenuation structure of the East Rift Zone and south flank of Kilauea Volcano, Hawaii, *Bull. Seismol. Soc. Am.*, 94, 1430–1440.

Julian, B. R., A. Ross, G. R. Foulger, and J. R. Evans (1996), Three-dimensional seismic image of a geothermal reservoir, The Geysers, California, *Geophys. Res. Lett.*, 23, 685–688.

Koulakov, I. (2009), LOTOS code for local earthquake tomographic inversion, benchmarks for testing tomographic algorithms, *Bull. Seismol. Soc. Am.*, 99, 194–214.

Lomax, A., A. Zollo, P. Capuano, and J. Virieux (2001) Precise absolute earthquake location under Somma-Vesuvius volcano using a new three-dimensional velocity model, *Geophys. J. Int.*, 146, 313–331.

Margaris, B. N., and D. N. Boore (1998) Determination of $\Delta\sigma$ and κ_0 from response spectra of large earthquakes in Greece, *Bull. Seismol. Soc. Am.*, 88, 170–182.

Michelini, A., and T. V. McEvilly (1991), Seismological studies at Parkfield, I, Simultaneous inversion for velocity structure and hypocentres using cubic b-splines parameterization, *Bull. Seismol. Soc. Am.*, 81, 524–552.

Mulargia, F., and S. Tinti (1985), Seismic sample areas defined from incomplete catalogues: An application to the Italian territory, *Phis. Earth Planet. Inter.*, 40, 273–300.

Nakajima, J., and A. Hasegawa (2003), Tomographic imaging of seismic velocity structure in and around the Onikobe volcanic area, northeastern Japan, implications for fluid distribution, *J. Volcanol. Geotherm. Res.*, 127, 1–18.

Nolet, G. (2008), *A Breviary of Seismic Tomography, Imaging the Interior of the Earth and Sun*, 1st ed., 344 pp., Cambridge Univ. Press, New York.

Orsi, G., S. de Vito, and M. Di Vito (1996), The restless, resurgent Campi Flegrei nested caldera (Italy), Constraints on its evolution and configuration, *J. Volcanol. Geotherm. Res.*, 74, 179–214.

Patanè, D., G. Barberi, O. Cocina, P. De Gori, and C. Chiarabba (2006), Time-resolved seismic tomography detects magma intrusions at Mount Etna, *Science*, 313, 821–823.

Pujol, J., and R. Aster (1990), Joint hypocentral determination and the detection of low-velocity anomalies. An example from the Phlegraean Fields earthquakes. *Bull. Seismol. Soc. Am.*, 80(1), 129–139.

Saccorotti, G., S. Petrosino, F. Bianco, M. Castellano, D. Galluzzo, M. La Rocca, E. Del Pezzo, L. Zaccarelli, and P. Cusano (2007), Seismicity associated with the 2004–2006 renewed ground uplift at Campi Flegrei Caldera, Italy, *Phys. Earth Planet. Inter.*, 165, 14–24.

Scandone, R., F. Bellucci, L. Kirer, and G. Rolandi (1991), The structure of the Campanian Plain and the activity of tje Napolitan volcanoes, *J. Volcanol. Geotherm. Res.*, 48, 1–31.

Sato, H., and M. C. Fehler (1998), *Seismic Wave Propagation and Scattering in the Heterogenous Earth*, 1st ed., 308 pp., Springer, New York.

Scarpa, R., F. Tronca, F. Bianco, and E. Del Pezzo (2002), High resolution velocity structure beneath Mount Vesuvius from seismic array data, *Geophys. Res. Lett.*, 29(21), 2040, doi:10.1029/2002GL015576.

Schmeling, H. (1985), Numerical models on the influence of partial melt on elastic, anelastic and electric properties of rocks. Part I, Elasticity and anelasticity, *Phys. Earth Planet. Inter.*, 41, 34–57.

Schurr, B., G. Asch, A. Rietbrock, R. Trumbull, and C. Haberland (2003), Complex patterns of fluid and melt transport in the central Andean subduction zone revealed by attenuation tomography, *Earth. Planet. Sci. Lett.*, 215, 105–119.

Sudo, Y., and L. S. L. Kong (2001), Three-dimensional seismic velocity structure beneath Aso Volcano, Kyushu, Japan, *Bull. Volcanol.*, 63, 326–344.

Takei, Y. (2002), Effect of pore geometry on V_P/V_S: From equilibrium geometry to crack, *J. Geophys. Res.*, 107(B2), 2043, doi:10.1029/2001JB000522.

Todesco, M., G. Chiodini, and G. Macedonio (2003), Monitoring and modelling hydrothermal fluid emission at La Solfatara (Phlegrean Fields, Italy). An interdisciplinary approach to the study of diffuse degassing, *J. Volcanol. Geotherm. Res.*, 125, 57–79.

Vanorio, T., J. Virieux, P. Capuano, and G. Russo (2005), Three-dimensional tomography from P wave and S wave microearthquake travel times and rock physics characterization of the Campi Flegrei Caldera, *J. Geophys. Res.*, 110, B03201, doi:10.1029/2004JB003102.

Villaseñor, A., H. M. Benz, L. Filippi, G. De Luca, R. Scarpa, G. Patané, and S. Vinciguerra (1998), Three-dimensional P-wave velocity structure of Mt. Etna, Italy, *Geophys. Res. Lett.*, *25*, 1975–1978.

Walck, M. (1988), Three-dimensional Vp/Vs variations for the Coso region, California, *J. Geophys. Res.*, *93*, 2047–2052.

Zollo, A., P. Capuano, and M. Corciuolo (Eds.) (2006), *Geophysical Exploration of the Campi Flegrei* (*Southern Italy*) *Caldera's Interiors, Data, Methods and Results*, Grup. Naz. per la Vulcanol., Naples, Italy.

Zollo, A., N. Maercklin, M. Vassallo, D. Dello Iacono, J. Virieux, and P. Gasparini (2008), Seismic reflections reveal a massive melt layer feed-ing Campi Flegrei caldera, *Geophys. Res. Lett.*, *35*, L12306, doi:10.1029/2008GL034242.

F. Bianco, E. Del Pezzo, and L. De Siena, Istituto Nazionale di Geofisica e Vulcanologia, Sezione di Napoli, Via Diocleziano 328, I-80124 Naples, Italy. (francesca.bianco@ov.ingv.it; edoardo.delpezzo@ov.ingv.it; luca.desiena@ov.ingv.it)